ADVANCED ENERGY MATERIALS
www.advenergymat.de

Interfacial Embedding for High-Efficiency and Stable Methylammonium-Free Perovskite Solar Cells with Fluoroarene Hydrazine

Dhruba B. Khadka, Yasuhiro Shirai,* Masatoshi Yanagida, Terumasa Tadano, and Kenjiro Miyano*

Perovskite solar cells (PSCs) with state-of-the-art efficiencies contain thermally unstable methylammonium (MA). Here, interfacial passivation with pentafluorophenylhydrazine (5F-PHZ) to fabricate efficient and stable MA/Br-free PSCs is introduced. The 5F-PHZ surface treatment quenches the PbI_2 and δ-perovskite phase formed in the pristine film. The surface passivation ameliorates the film chemistries at the surface with modulation of interface band alignment as a consequence of halogen bonding with fluoroarene moieties or $NH–NH_2$ terminals. This results in a much longer carrier lifetime with the passivation at the surface and grain boundaries trap centers. As a result, it boosts the power conversion efficiency (PCE) (area ≈ 1 cm^2) from 18.10% to 22.29% (V_{OC} ≈ 1.096–1.178 V) with superior operational thermal stability. A certified PCE of 21.01% with a large area of ≈1.026 cm^2 is also achieved. It is found that the surface passivation forms an interfacial embedded layer subsequent to attenuation of defect densities and suppression of ion migration, which is supported by density-function-theory calculation. Importantly, this approach is effective in enhancing the PCE of narrow and wide bandgap perovskite systems. Thus, this work opens up a new technique for interface modulation with fluoroarene functional derivatives to achieve superior device performance and stability.

1. Introduction

The power conversion efficiency (PCE) of 3D halide perovskite solar cells (PSCs) has soared to above 25% benefiting from their exceptional optoelectronic properties.[1,2] However, this has imposed challenges for its practical application due to its lacking stability under heat and light stress as well as susceptibility to a humid atmosphere.[3–6] The surface passivation approach has been widely employed in PSCs to improve the device parameters as well as stability as a consequence of mitigating the defect activities,[7] modifying interfacial band alignments,[8] improving carrier extraction dynamics,[9] and enhancing moisture tolerability.[10,11]

Several functional molecules have been employed for passivating materials at the interfaces[12,13] or additives in the perovskite precursor solution.[7,14,15] Multiple reports have documented the composition engineering of perovskite bulk layer by adding components such as isovalent ions[3,16,17] and organic functional additives (piperidinium salt, formamidine disulfide, 5-ammonium valeric acid iodide, etc.)[15,18,19] which contributes to phase stability and defect passivation. On the other hand, the functional additives with varying alkyl or phenyl chains have been used to mitigate grain boundaries (GBs) recombination of the polycrystalline nature of HaP films, and the interfacial loss at the surface by forming a thin capping layer of low dimensional perovskite.[10,11,20] It has been documented that the alkyl chain length of alkylammonium iodide deposited on the surface of 3D-HaP (FAMA) affects PCE and stability.[21] A wide-bandgap lead oxysalt was used for a surface treatment of perovskite that demonstrated a reduction of the defect density resulting in superior PCE with superior stability. Similarly, Yang et al. have reported multifunction passivation using n-butylammonium bromide which effectively mitigates the recombination centers in the bulk and at the interface of the perovskites (different bandgaps) enhancing the device efficiency with a low voltage deficit < 0.4 V coupled with superior operational stability.[8] Besides these, many groups used mitigating materials having various functional characteristics such as ionic compounds[19,22–24] and molecular modulators[25–28] for enhancing the performance and stability of PSCs. Few fluorous organic functional materials have also been reported to be excellent for mitigating recombination and humidity effect due to the high electronegativity of fluorine branches.[11,29–32] Gratzel

D. B. Khadka, Y. Shirai, M. Yanagida, K. Miyano
Photovoltaic Materials Group
Center for GREEN Research on Energy and Environmental Materials
National Institute for Materials Science (NIMS)
1-1 Namiki, Tsukuba 305-0044, Japan
E-mail: khadka.b.dhruba@nims.go.jp; shirai.yasuhiro@nims.go.jp
T. Tadano
Research Center for Magnetic and Spintronic Materials
National Institute for Materials Science (NIMS)
1-2-1 Sengen, Tsukuba 305-0047, Japan
The ORCID identification number(s) for the author(s) of this article can be found under https://doi.org/10.1002/aenm.202202029.

DOI: 10.1002/aenm.202202029

and co-workers have used the penta[10] or tetra fluoro[33] in phenethyl chain as passivating materials for the improvement in device performance and its stability under a higher humid atmosphere. Hagfeldt and co-workers have demonstrated the effect of mixed salt passivation in the 3D HaP (mixed cations and anions) using ammonium iodide derivatives with the F-substituted alkyl chain of varying lengths in the presence of formamidinium bromide resulting in an improved PCE and operational stability.[34] Noting these advantageous functional characteristics, it could be of great interest to explore the fluorinated functional materials to resolve the issue related to PSCs.

In this work, we introduced a fluoroarene anchored functional material; pentafluorophenylhydrazine (5F-PHZ) for interface treatment onto the 3D-MA/Br-free HaP film with the precursor formulation of $FA_{0.84}Cs_{0.12}Rb_{0.04}PbI_3$ (denoted as regular bandgap HaP [RB-HaP]; $E_g \approx 1.52$ eV). This approach enhanced the device performance as high as 22.29% ($A \approx 1\ cm^2$) with superior operational stability. The 5F-PHZ treatment has shown a significant impact on the morphology, interface chemistry, and optoelectronic properties of HaP films. It suppressed trap states in the bulk and on the 3D surface resulting in a longer carrier lifetime and enhanced photovoltaic characteristics. We have also extended this approach for MA-free wide bandgap ($FA_{0.84}Cs_{0.12}Rb_{0.04}Pb(I_{0.64},Br_{0.36})_3$) (WB-HaP; $E_g \approx 1.72$ eV) and low bandgap Pb-Sn mixed HaP (NB-HaP; $E_g \approx 1.25$ eV) to confirm its propitious merits for surface passivation. This work has also unraveled insight into the synergetic effect in film growth and photo-physics of PSCs with compositional and bandgap variation.

2. Results and Discussion

Figure 1a–c depicts the schematic illustration of the surface treatment of MA-free HaP film with 5F-PHZ in isopropanol as an interface passivation layer (IPL) solution. The scanning electron microscopy (SEM) images (Figure $1d_1$–d_4 and Figure S1, Supporting Information) show that 5F-PHZ treatment affects the film growth with a slight increase in grain size with a faint indication of the formation of an overlayer on the perovskite grain domain. The overlayer surface features are predominately observed on the film treated with a higher concentration of 5F-PHZ. This could be a consequence of adsorption of 5F-PHZ on HaP film's surface which unevenly forms a 2D phase interacting with the lead iodide as observed in a report by Gratzel and co-workers.[10] The UV-vis absorption spectra (Figure 1e, inset) indicate that the surface passivation with 5F-PHZ treatment does not affect the absorption spectra of HaP films. The PL spectra (Figure 1f) also do not show any notable feature except a slight blue shift of the PL characteristic peak (≈819–817 nm).

We measured X-ray diffraction (XRD) patterns of the control and passivated HaP films to investigate crystal growth. The 5F-PHZ passivated HaP films reveal some interesting features in XRD results (Figure 1g,h). The control film grows with the dominant (110) plane of α-phase of FA- perovskite along with weak peaks of δ-Cs/$RbPbI_3$ phase and residual PbI_2 at ≈10° and 12.7°, respectively. As we mixed A-site substituent with a large difference in atomic size (Rb, Cs, FA; ≈152, 167, and 253 pm), there is a possibility of formation of δ-perovskite phase. These observations agree with other reports.[3,15,35] Interestingly, the characteristic diffraction peaks of δ-perovskite phase and residual PbI_2 almost disappeared on the 5F-PHZ treated HaP films indicating growth of better film quality. Moreover, an additional XRD response appeared at ≈8.4° on the film with a higher concentration of 5F-PHZ (≥2 mol%) suggesting the formation of a 2D phase of $(5F\text{-}PHZ)_2PbI_4$ with the interaction of residual PbI_2 and suppression of formation of δ- perovskite.[10] For confirmation, we prepared HaP films by mixing 5F-PHZ in a perovskite precursor solution. It clearly demonstrated the formation of 2D-phases in crystallized film in XRD patterns and absorption spectra as depicted in Supporting Information (Figure S2, Supporting Information). Importantly, it is observed that the spurious phases (PbI_2 residual and δ-perovskite phase) observed on the control film are suppressed much more effectively in the HaP film with 5F-PHZ surface treatment rather than in HaP films prepared by using precursor solution mixing 5F-PHZ in HaP precursor (Figure S2, Supporting Information). This observation underlines the importance of the 5F-PHZ treatment from the surface for improving perovskite film quality.

To examine the effect of 5F-PHZ treatment on photovoltaic performance, we fabricated complete devices adopting the device architecture as depicted in **Figure 2**a. The current density-voltage (J–V) characteristics of control and 5F-PHZ treated (3 mol%) champion devices are given in Figure 2b (Figure S3, Supporting Information, varying 5F-PHZ concentrations) with a large device area of ≈1 cm^2 (device photo; Figure S4, Supporting Information). The J–V curve with 5F-PHZ treated HaP has negligible hysteresis. Compared with the control device yielding *PCE* of 18.10%, we achieved *PCE* as high as 22.29% with an increase in $V_{OC} \approx 1.096$ to 1.178 V, $J_{SC} \approx 22.88$ to 24.51 $mAcm^{-2}$, and *FF* ≈72.2% to 77.2% (**Table 1**). This improvement in *PCE* is obtained with a small V_{OC} deficit of 0.338 V. Considering the little difference between the bandgaps of the control and 5F-PHZ treated HaP films, the V_{OC} enhancement is attributed to the reduction of non-radiative recombination. It has been reported that the fluorinated aromatic rings minimize the iodine vacancy, surface defect, and migration with strong halogen bonding.[33] Similarly, the nitrogen sites enhance the adhesion to the perovskite surface with $NH\text{–}NH_2$ terminals, which is propitious for defect passivation. It will be discussed in the succeeding paragraph. The statistics of device parameters as a function of the 5F-PHZ concentration depicted in Figure 2c (Figure S5, Supporting Information) implicate a better reproducibility. The device with a higher concentration of 5F-PHZ seems to be less efficient with lowering V_{OC} and *FF*. This could be a consequence of unevenly formed 2D-phases on the surface of HaP films (Figure $1d_4$ and Figure S1, Supporting Information). Our device result was validated with a certified *PCE* of ≈21.01% of a large area of ≈1.026 cm^2 under standard conditions (accredited independent photovoltaic test laboratory, AIST PV Lab, Japan). The official report is included in Supporting Information (Figure S6, Supporting Information). Note that it is a record-level PCE for MA/Br-free inverted p-i-n PSC configuration for a large area of >1 cm^2. Here, we also have listed the results of certified PCE of PSCs with a large area of >1 cm^2, and where our 5F-PHZ device compares favorably amongst the reports (Table S1, Supporting Information).

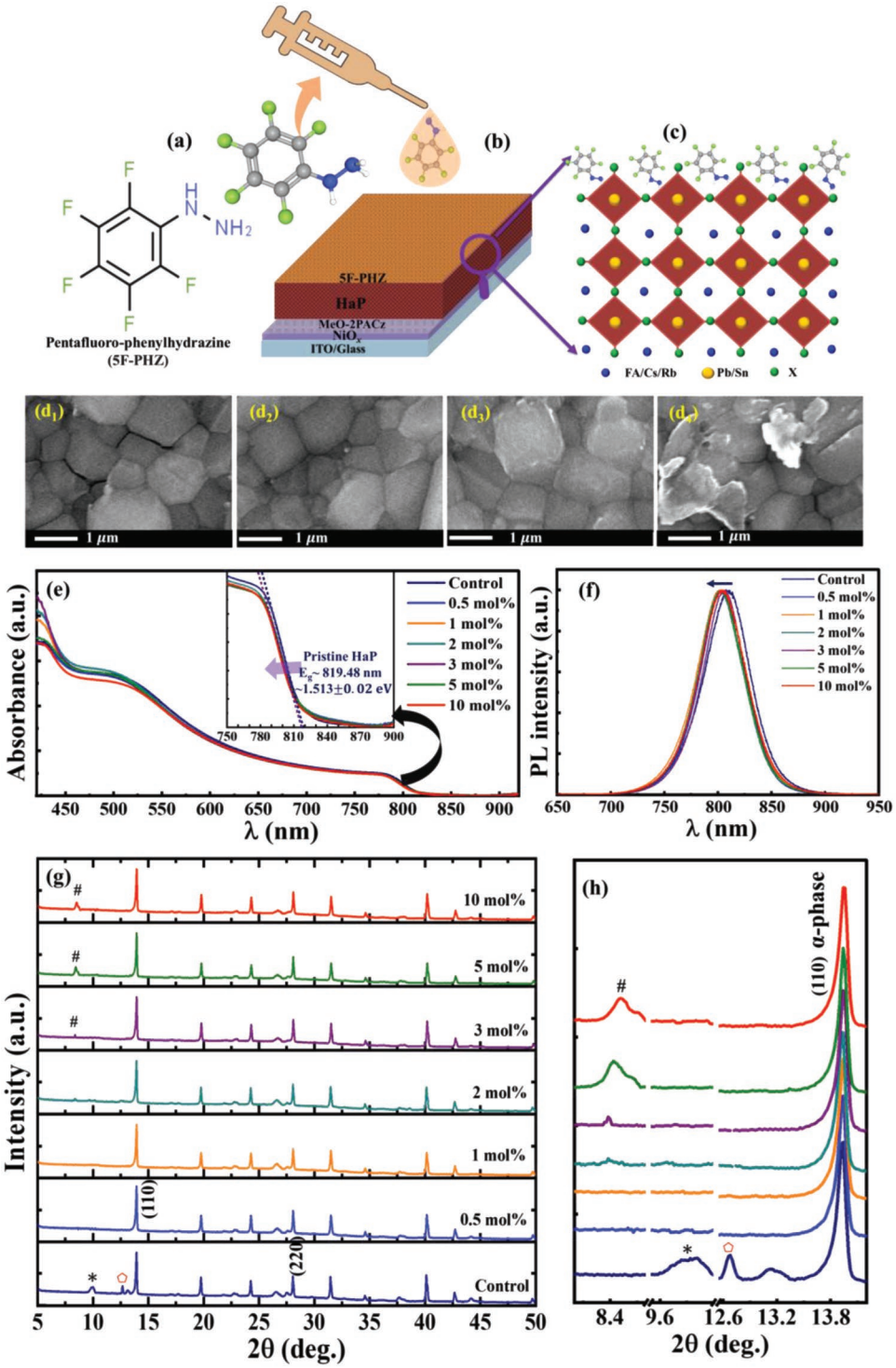

Figure 1. Schematic illustration of surface treatment; a) fluoroarene anchored functional material; 5F-PHZ, b) device architecture, c) schematic of interfacial interaction of 5F-PHz and HaP surface, d_1–d_4) SEM images of HaP films with 5F-PHZ treatment with different concentrations, e) absorption spectra, f) PL spectra, and g,h) XRD results of without and with 5F-PHZ treated HaP films. Here, ⬠- PbI_2 residual, ⁎- δ-perovskite phase, # -2D phase with 5F-PHZ.

Figure 2d gives the external quantum efficiency (*EQE*) spectra of the control and 5F-PHZ treated (3 mol%) champion device. The *EQE* spectrum shows a higher photoresponse in the absorber layer band edge regime (650 $\lambda < 775$ nm) and HaP/CTL interface regime in a lower wavelength (450$\lambda >$ 330 nm).[36] This indicates an improvement in bulk as well as interface quality of PSCs with 5F-PHZ treatment which also supports the improvement in film quality. Note that the J_{SC} values integrated

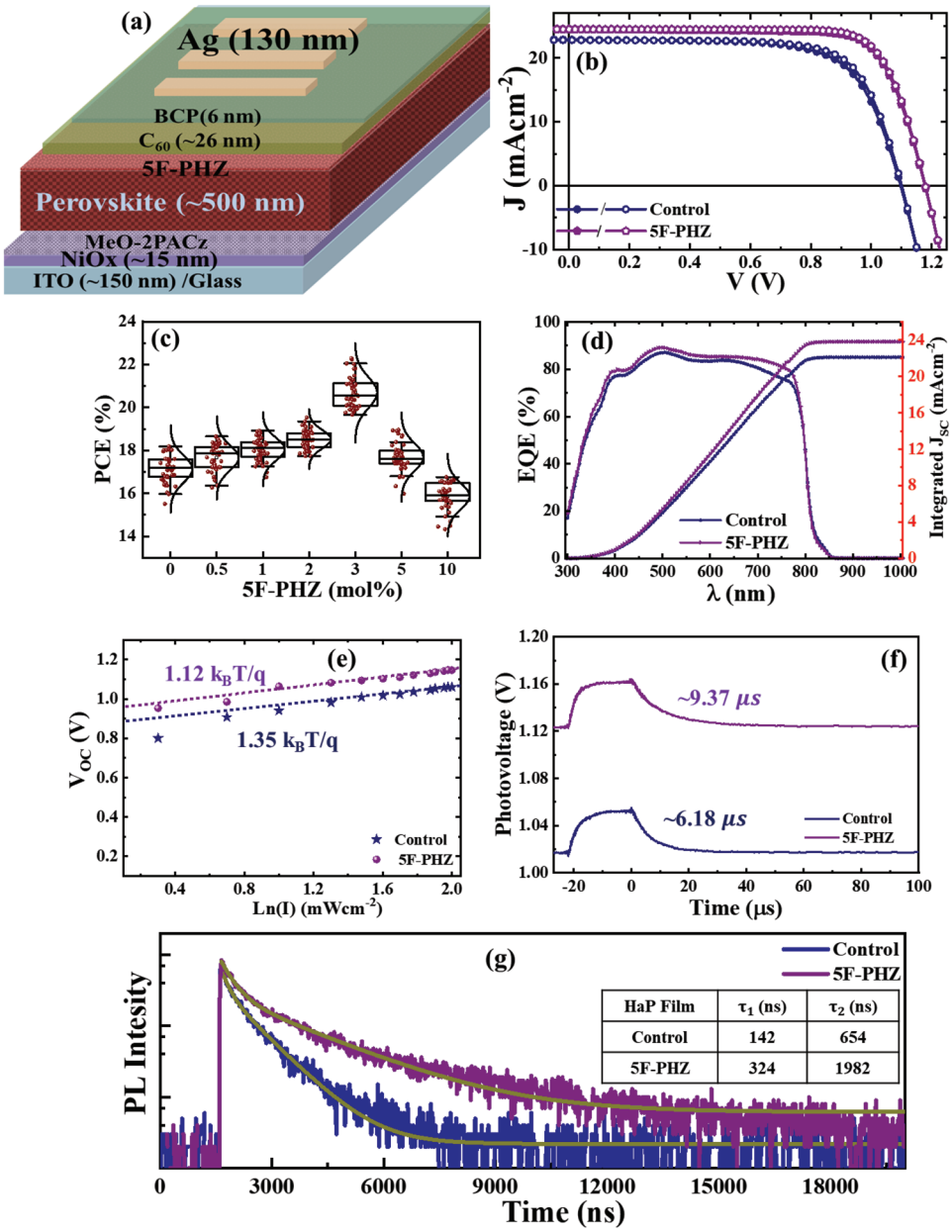

Figure 2. a) Schematics of the device structure. b) *J–V* curves of the control and 5F-PHZ treated (optimal concentration; $x = 3$ mol%) device; (▼forward/s reverse scan direction). c) Statistics of *PCE* of the PSCs with surface treatment with varying concentrations of 5F-PHZ solution. These data consist of 40 devices from five batches. d) *EQE* spectra. e) Light intensity dependence of V_{OC}. f) TPV decay curves of the control and 5F-PHZ treated devices. g) TRPL decay spectra of corresponding films.

Table 1. Photovoltaic parameters and V_{OC} deficit of the best performing PSCs (without and with 5F-PHZ treatment) using different perovskite systems (RB, WB, and NB). E_g^a estimated from *EQE* analysis of respective devices. The average values of *PCE* and standard deviation are given in parentheses.

Perovskite composition	Condition	E_g^a [eV]	J_{SC} [mAcm^{-2}]	V_{OC} [V]	*FF*	*PCE* [%]	(E_g^a/q -V_{OC}) [V]
$Rb_{0.04}Cs_{0.12}FA_{0.84}PbI_3$ (RG-HaP)	Control	1.514	22.88	1.096	0.722	18.10 (17.26 ± 0.64)	0.418
	5F-PHZ	1.516	24.51	1.178	0.772	22.29 (21.03 ± 0.65)	0.338
$RbCsFAPb(I_{0.64},Br_{0.36})_3$ (WG-HaP)	Control	1.721	18.24	1.241	0.739	16.73 (15.62 ± 0.71)	0.480
	5F-PHZ	1.725	19.28	1.283	0.765	18.92 (18.32 ± 0.42)	0.442
$Cs_{0.05}MA_{0.1}FA_{0.85}(Pb_{0.5},Sn_{0.5})I_3$ (NG-HaP)	Control	1.246	30.72	0.758	0.722	16.81 (15.23 ± 0.98)	0.488
	5F-PHZ	1.246	31.16	0.831	0.747	19.34 (18.74 ± 0.57)	0.415

from *EQE* spectra are 22.12 and 23.86 mAcm^{-2} which are in close agreement with the J_{SC} from *J–V* curves. Moreover, the bandgaps (E_g) estimated from *EQE* spectra (Figure S7a, Supporting Information) (1.514 for control and 1.516 eV for HaP with 5F-PHZ treatment) are also consistent with the E_g obtained from the PL (Figure 1f) and absorption spectra (Figure S7b, Supporting Information).

To gain insight into the device improvement, we studied the characteristic response of the control and 5F-PHZ devices. In Figure 2e, we investigated the charge recombination behavior by analyzing the light-intensity-dependent V_{OC} of the devices. The control device shows a slope of 1.35 $k_BT\ q^{-1}$ which is higher than the device with HaP-5F-PHZ treatment (1.12 $k_BT\ q^{-1}$) which indicates a reduction in trap-assisted recombination in PSCs.[18] The transient photovoltage (TPV) was recorded as depicted in Figure 2f by modulating V_{OC} with transient illumination. The analysis of TPV decay signals demonstrates a carrier lifetime of 6.18 µs for the control device which is longer for the 5F-PHZ treated device (9.37 µs), indicating well consistency with device performance as a result of defect passivation. It is in line with other reports.[18,37]

To add further detail, the time-resolved photoluminescence (TRPL) spectra (Figure 2g) were fitted with the widely used bi-exponential decay equation; $I(t) = A_1 e^{\frac{-(t-t_0)}{\tau_1}} + A_2 e^{\frac{-(t-t_0)}{\tau_2}}$, where the decay times; τ_1 is mainly associated with the nonradiative recombination at the interface and τ_2 accounts for the radiative recombination at the bulk layer. The 5F-PHZ treated HaP film shows a significantly longer carrier lifetime ($\tau_1 \approx 324$ ns and $\tau_2 \approx 1982$ ns) compared to that of the control film ($\tau_1 \approx 144$ ns and $\tau_2 \approx 654$ ns). It corroborates that the recombination pathways at the interface as well as bulk have been suppressed with the 5F-PHZ treatment indicating amelioration of surface chemistry and attenuation of trap densities in the HaP bulk with halogen bonding modulation and suppression of ionic defect.[38]

To assess the surface energy status, we performed UV photoelectron spectroscopy (UPS). **Figure 3**a exhibits the cutoff energy (C_{utoff}) in the high-binding energy region corresponding to work function (ϕ) and the onset energy (E_i) (difference between the valence band and Fermi level ($\Delta E_{F,V} = E_V - E_F$)) extracted from the UPS spectra. These values are found to be slightly increased for the HaP film with 5F-PHZ treatment. Figure 3b depicts the band structure combining optical bandgap (Figure S7b, Supporting Information). It shows an increase in work function with a downshift of E_V (0.30 eV) and E_C (0.29 eV) levels that reduce the interfacial band offset with NiO*x*/MeO-2PACz and C_{60}.[39,40] It ascribes the interfacial band modification with 5F-PHZ treatment which is propitious for the effective carrier transfer as well as other device parameters.

Furthermore, we performed X-ray photoelectron spectroscopy (XPS) measurements to explore the surface chemistry of the HaP films. The XPS spectra of C 1s (Figure 3c) show a characteristics peak centered at ≈289.4 eV corresponds to H–C–F bonding.[41] F 1s core spectra (Figure 3d) centered at ≈688 eV also confirms the presence of 5F-PHZ on the HaP film. The 5F-PHZ treated film exhibits a shift of XPS characteristic peak of Pb 4f and I 3d (≈0.14 and 0.15 eV; Figure 3e and Figure S8a, Supporting Information) towards higher binding energy suggesting stronger ionic bonding induced with 5F-PHZ on the film surface. The XPS depth profiling of fluorine (F) (Figure S9a, Supporting Information) shows the F 1s signal remains for 30 s etching (≈6 nm) and disappears after 90 s etching (≈20 nm). It suggests the 5F-PHZ material could have been buried up to a ≈10 nm-thin layer. The XPS peaks corresponding to the Cs 3d and Rb 3d core level (Figures S8 and S9, Supporting Information) in the 5F-PHZ treated HaP film reveal a slight asymmetry towards higher binding energy indicating a stronger binding interaction with fluorine-rich bonding branches. Furthermore, the elemental core characteristics of HaP with 10 mol% 5F-PHZ treatment (Figure S9b–f, Supporting Information) consolidate its existence and beneficial aspects of surface treatment with broadening and blue shifting of XPS characteristic peak.

To investigate the depth-dependent distributions of 5F-PHZ in the HaP film, we conducted time-of-flight secondary ion mass spectrometry (ToF-SIMS) measurements on the control and 5F-PHZ treated HaP films. The selected ionic species for respective layers are displayed in Figure 3f,g. The ToF-SIMS profiles reveal almost identical ionic distribution in the bulk HaP films except for the F^- ion profile. The F^- ion from 5F-PHZ (Figure 3g) shows a significantly higher signal on the surface of HaP film indicating its rich distribution on the surface of 3D HaP. We also observed a slopy gradient of the F^- ion with an intensity of over two orders of magnitude lower than that on the surface indicating its diffusion to the bulk HaP. It is attributed to the diffusion of 5F-PHZ through the grain boundaries that could passivate the defect in the bulk or at grain boundaries. Importantly, although the ionic gun for digging is different, the F^- ion profile in ToF-SIMS also supports the XPS depth profile of the F 1s signal (Figure, S9a, Supporting Information).

To probe the interfacial structure developed with the 3D HaP host, we studied the cross-sectional transmission electron microscopy (TEM) analysis. As depicted in Figure S10, Supporting Information, the STEM images of the control and 5F-PHZ treated devices show a distinct feature at the interface of HaP/C_{60} (Figure S10a_2,b_2, Supporting Information). The HR-TEM images at the interface of the 5F-PHZ treated device exhibit (Figure S10b_3, Supporting Information) a wide interplanar d-space confirming the existence of a 2D phase at the interface or buried in 3D HaP host film. Albeit uneven distribution of the thin 2D phase at the HaP/C_{60} interface, it effectively modifies the chemistries at surface or grain boundaries and interfacial band structure. This result is consistent with other reports on interface passivation.[8,42] Regarding the elemental distribution, the elemental mappings (Figure S11, Supporting Information) of corresponding devices across the cross-sectional STEM images do not show a significant difference within the resolution limit. These observations substantiate that the 5F-PHZ treatment plays a vital role in ameliorating the device quality with interfacial structural modification.

To further analyze the 5F-PHZ passivation effect, we studied capacitance spectroscopy. The capacitance-voltage (*C–V*) data were analyzed to get the Mott–Schottky (*M–S*) plot and carrier profile (N_{CV}) as in the reports.[17,43–45] The *M–S* plots (**Figure 4**a) exhibit fully depleted curves for $V > V_D$ indicating intrinsic junction. Interestingly, small hysteresis on the *M–S* curve at the vicinity of V_D for the control device almost disappeared for the 5F-PHZ treated device which could be due to the reduction in

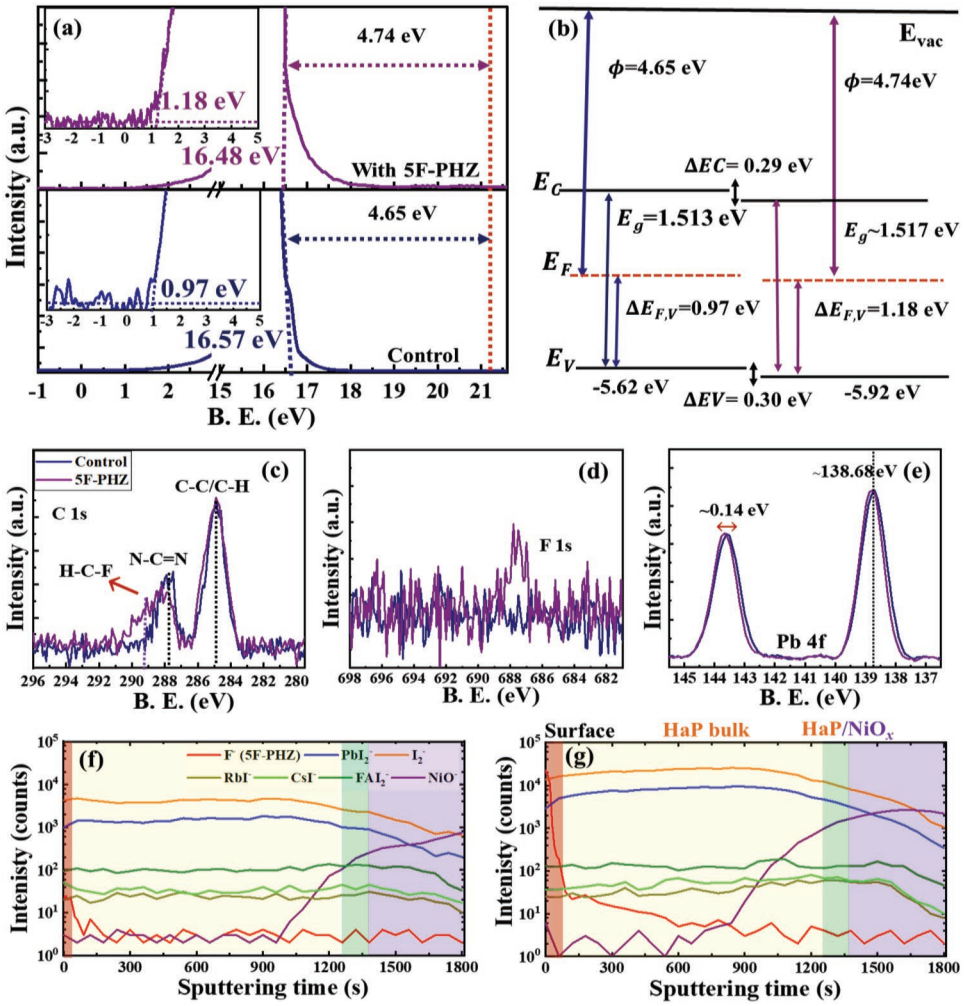

Figure 3. a) UPS spectra of the RB-HaP films; control and 5F-PHZ additive; the photoemission cutoff energy (right-side) (left side and inset; valence band spectra with the energy difference between the valence band maximum [E_V] and the Fermi level [E_F]). b) Energy band schematics extracted from UPS spectra. XPS-spectra analysis; c) C-1s core, d) F-1s core, and e) Pb-4f core. ToF-SIMS depth profiles of the f) control and g) 5F-PHZ treated films. The red, yellow, green, and magenta shaded regions indicate the surface, bulk, perovskite/HTL, and HTL (NiO_x), respectively.

ionic polarization at the interface. The diffusion potential (V_D) increases from 0.984 to 1.12 V for the device with 5F-PHZ treatment which is in line with the increase in the V_{OC}. Figure 4b displays the carrier profile calculated from C–V data (N_{CV}) that consists of the free carrier and defect density. It shows a wide U-shaped carrier profile with a similar bulk carrier density (N_{CV}^{B}) of ≈4.12 × 10^{15} cm^{-3}. However, the edge of the carrier profile that accounts for the interface defect profile ($N_{CV}^{IF} \approx 13.38 \times 10^{17}$ for control to ≈2.15×10^{17} cm^{-3} for the 5F-PHZ treated device) is attenuated approximately by five times for the 5F-PHZ treated PSC. It substantiates that the 5F-PHZ mitigates recombination centers which improve the device parameter.

To reveal the defect profile more quantitatively, we investigated thermal capacitance spectroscopy (TCS), an effective technique for estimating both the energy level of trap states and trap density in different PV systems (kesterite solar cells,[46] organic solar cells,[47] and PSCs[48,49]). The capacitance-frequency (C–f) spectra under dark in Figure 4c show a slightly higher value in the plateau regime (1 to 100 kHz) that arises from the HaP layer accounting for defect dynamics. At the same time, the capacitance at a lower frequency, which stems from the interfacial charge accumulation or ionic polarization, is much steeper for the control device. It indicates suppression of interfacial charge accumulation for the device with 5F-PHZ treatment. We analyzed the temperature-dependent capacitance-frequency (C–f–T) spectra to calculate the trap energy state (E_t). E_t is calculated from the Arrhenius plot[50] $\left\langle ln\left(\frac{\omega_o}{T^2}\right) = \frac{-E_t}{k_B T} + ln\vartheta_o \right\rangle$, where ω_o is characteristic resonance frequency extracted from C–f–T inflection point (Figure S12, Supporting Information) and ϑ_0 is the emission factor comprising all the temperature-independent parameters. From the Arrhenius plot (Figure 4d), we found a shallower trap level in the 5F-PHZ passivated device, that is, $E_{t1}, E_{t2} \approx 0.254, 0.405$ eV in the control device and $E'_{t1}, E'_{t2} \approx 0.237, 0.378$ eV in the 5F-PHZ treated device. The defect density profiles (Figure 4e,f) are calculated from the equation,[50,51] $N_t(E_\omega) = \frac{-V_D}{qW}\left(\frac{\omega}{k_B T}\frac{dC}{d\omega}\right)$, V_D and W are the

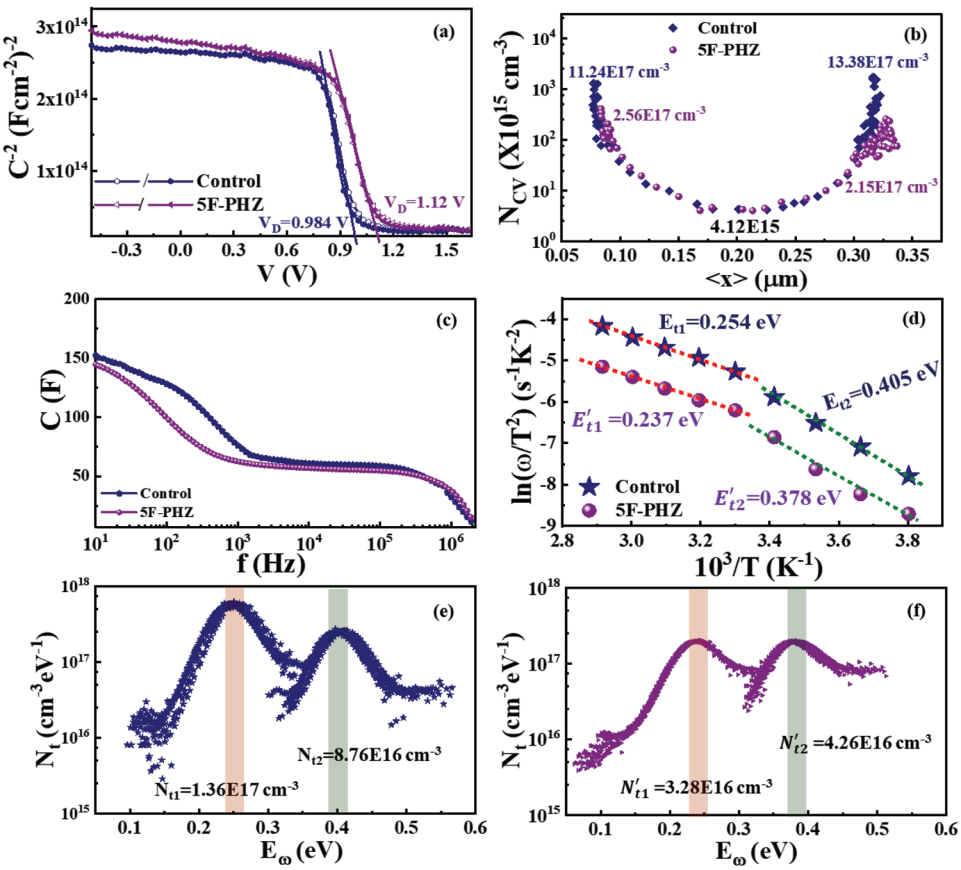

Figure 4. Capacitance-voltage (*C–V*) characteristics of devices; a) Mott–Schottky plots (▼forward/s reverse scan direction), b) carrier profile extracted from *C–V* analysis, c) C–f response, d) the Arrhenius plots, and e,f) defect density (N_t) profiles of the respective devices.

diffusion potential and the space charge region (SCR), extracted from *C–V* data, q is the elementary charge, and ω is applied frequency. The integrated defect densities for the control device (N_{t1}, $N_{t2} \approx 1.36 \times 10^{17}$, 8.76×10^{16} cm^{-3}) are attenuated for the 5F-PHZ treated device (N'_{t1},$N'_{t2} \approx 3.28 \times 10^{16}$, 4.26×10^{16} cm^{-3}). Although these defect densities are much higher than a single crystal (10^{10} cm^{-3}), the trap densities in a thin film perovskite have been reported in the range of 10^{16}–10^{19} cm^{-3}.[40,52] Our calculations also fall within these reports. It indicates much room to lower down the traps for better film quality. The defect densities (N_{t2}) primarily assigned for defects in the bulk layer are found to be reduced by half in the 5F-PHZ treated device indicating improved bulk quality. Regarding, the density of shallower trap defects (N_{t1}), which is assigned to traps at the surface or GBs in control films, is four times higher than in the 5F-PHZ treated devices. This corroborates that the 5F-PHZ may diffuse into the GBs to passivate the defect states due to stronger non-covalent interaction of fluoroarene moieties or NH–NH$_2$ terminals at the perovskite surface. It well supports the benignant characteristics observed in the film as discussed in previous paragraphs. Thus, these results further consolidated that the 5F-PHZ treatment is effective to mitigate the defect chemistries at film surface, GBs as well as bulk.

The passivation effects by 5F-PHZ were also investigated by first-principles calculation based on density functional theory (DFT). **Figure 5**a compares the calculated density of states (DOS) of the pristine PbI$_2$-terminated slab and that of the slab with the I_{Pb} antisite defect on one side of the surface in accord with the previous DFT calculation.[54] The isosurface of the defect-state charge density depicted in Figure 5b shows that the defect level is localized around the defect site, which can work as a non-radiative recombination center. This defect state was mostly eliminated after passivating the defect site by 5F-PHZ (Figure 5a, bottom panel), which deteriorates the solar cell performance. Our calculation revealed that the 5F-PHZ ameliorates the perovskite film by attaching NH–NH$_2$ terminals on the film surface with angular orientation as depicted in Figure 5c. The defect passivation tendency with different molecular orientational attachments of 5F-PHZ is displayed in Figure S12, Supporting Information. The opposite site of the NH–NH$_2$ terminal of the 5F-PHZ molecule bonded to the perovskite surface is found to be most unstable and less effective for perovskite's surface passivation. To quantify the effectiveness of 5F-PHZ as a passivation molecule, we also calculated the desorption energy of a 5F-PHZ molecule on the defected surfaces and compared them with those of another fluoroarene-based molecule, 2,3,4,5,6-pentafluoroaniline (PHA), which has recently been used as a passivating additive for MAPbI$_3$.[32] The calculated desorption energies of a 5F-PHZ (PHA) were 1.23 (0.91) and 1.76 (0.76) eV on the I_{Pb}- and P_{bI}-defected surface, respectively, indicating that 5F-PHZ can form a more stable surface structure and thus superior to PHA. To test the theoretical

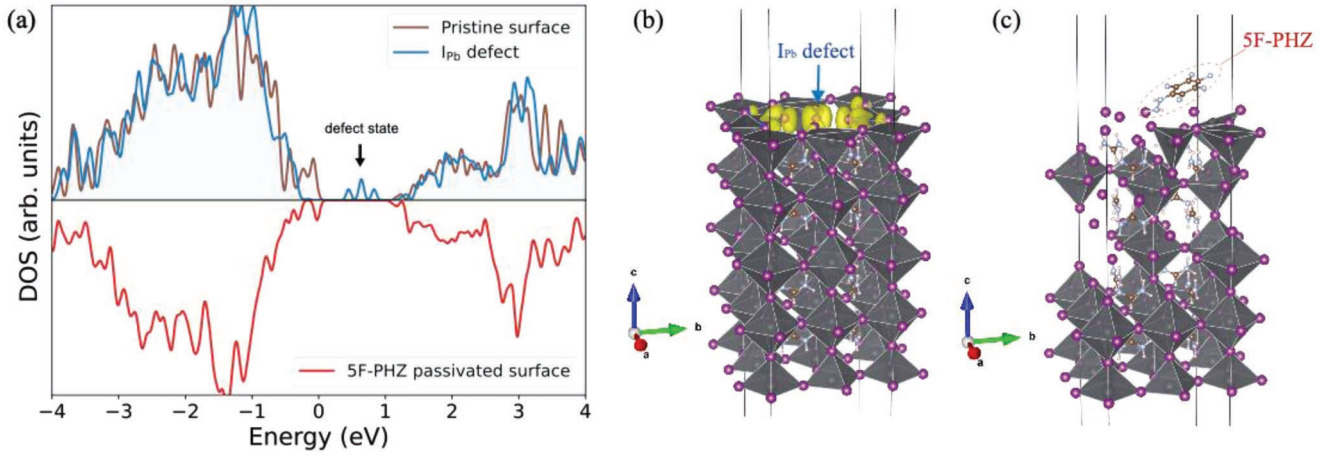

Figure 5. a) Calculated density of states (DOS) of PbI_2-terminated slab models with various surface conditions. b) The structure model of the PbI_2-terminated slab with an I_{Pb} antisite defect on one side of the surface. The isosurface of the charge density for the defect state is also shown. c) The optimized low-energy structure of a 5F-PHZ passivated surface. The figures in (b) and (c) were created using VESTA software.[53]

hypothesis, we prepared PSCs with PHA treatment and *J–V* results are depicted in supporting information (Figure S14 and Table S2, Supporting Information). We observed an improvement in the J_{SC} and *FF* for the device with PHA treatment but there is no significant enhancement in V_{OC} with reference to the control device. It implicates that PHA treatment is not as effective as the 5F-PHZ treatment for defect passivation in the bulk and on the surface of perovskite. Thus, the DFT results support the defect passivation properties of 5F-PHZ which results in improving device performance and stability.

The effectiveness of the passivation of 5F-PHZ treatment has also been tested in more perovskite systems having different E_g. In the narrow bandgap perovskite system (NB-HaP; $Cs_{0.05}MA_{0.1}FA_{0.85}(Pb_{0.5}, Sn_{0.5})I_3$, we fabricated the NB-PSCs of inverted structure as depicted in Figure S15a, Supporting Information. As displayed in Table S3, Supporting Information, the device with 5F-PHZ treatment ($E_g \approx 1.246 \pm 0.005$ eV; NB-HaP, Figure S15e,f, Supporting Information) at 3 mol% demonstrates a champion *PCE* of 19.34% with the figure of merits; $V_{OC} \approx 0.831$ V, $J_{SC} \approx 31.16$ mAcm^{-2}, and $FF \approx 0.747$. The control has a *PCE* of 16.81% ($V_{OC} \approx 0.758$ V, $J_{SC} \approx 30.72$ mAcm^{-2}, and $FF \approx 0.722$). These results are in the record-line of PCE for NB-PSCs using reduced MA in Pb-Sn mixed perovskite film.[55] The *J–V* and *EQE* data of respective devices are given in Figure S15b,c, Supporting Information. The diode ideality factor estimated from intensity-dependent V_{OC} shows a lower value for the device with 5F-PHZ treatment (1.46 to 1.22 $k_BT\ q^{-1}$; Figure S15d, Supporting Information) suggesting passivation of trap-assisted recombination. This is parallel to the results for RB-PSCs. The significantly enhanced device parameters are associated with a reduced V_{OC} deficit which is attributed to the amelioration of film surface chemistry, interface quality, and modification of interface alignment as discussed in regular bandgap HaP. This result validates the effectiveness of the 5F-PHZ treatment for NB-PSCs.

This method was also applied in wide-bandgap MA-free-PSCs, which are ideal wide-bandgap subcells for tandem PSCs. The device fabrication has been described in the experimental section. As reported in our earlier work for WB-PSC,[51] we used C_{60}-fused N-methylpyrrolidine-meta-dodecyl phenyl ($C_{60}MC_{12}$) as the ETL layer. As summarized in Table 1 and supporting information (Figure S16 and Table S4, Supporting Information), the wide-bandgap $FA_{0.84}Cs_{0.12}Rb_{0.04}Pb(I_{0.63}Br_{0.37})_3$ PSC (WB-HaP; $E_g \approx 1.72$ eV, extracted from *EQE* analysis, Figure S16c, Supporting Information); demonstrated a *PCE* of 18.92% with a significant increase in the V_{OC} of ≈1.283 V for the 5F-PHZ treated film adopting the device architecture (Figure S16a, Supporting Information). The control device has a *PCE* of 16.73%. The *J–V* curves and *EQE* spectra are given in Figure S16b,c, Supporting Information. This result shows a record V_{OC} with lowered V_{OC} deficit ≈0.480 to 0.442 V validating the benefit of 5F-PHZ treatment. Though there is much room for improvement, to the best of our knowledge, these values are in the range of the highest reported PCE for respective perovskite compositions. Moreover, a significant reduction of V_{OC} deficit (Table 1) is attributed to mitigation of non-radiative recombination and betterment in interface quality with 5F-PHZ treatment.[8]

Lastly, we monitored the operational stability of the control and 5F-PHZ devices (encapsulated) at the maximum power point tracking (MPPT) conditions under one sun irradiation in the ambient atmosphere at room temperature (RT) (RT~35%–40% RH) and elevated temperature (≈65 °C, equivalent to the roof temperature). As depicted in **Figure 6**a,b (Figure S17, Supporting Information), the 5F-PHZ passivated device demonstrated superior device stability. At RT, the *PCE* of the control device decreased to ≈73.50% of initial PCE in 500 h which significantly dropped to ≈27.82% in 500 h under thermal stress at ≈65 °C. While the device with 5F-PHZ treatment retained ≈92.52% and 83.68% of original PCE in 500 h at respective aging conditions. These results indicate that the device with 5F-PHZ treatment significantly improves the thermal stability which is benefited by interfacial halogen bonding modulation.[33] In addition, we also obtained the operational stability data under higher humidity (60%–65% RH) as shown in supporting information (Figure S18a, Supporting Information). The *PCE* of the device with 5F-PHZ treatment retained ≈82.18% of the initial PCE in 300 h. In comparison, the PCE of the control device quickly dropped to ≈41.62% of the original PCE in only 150 h.

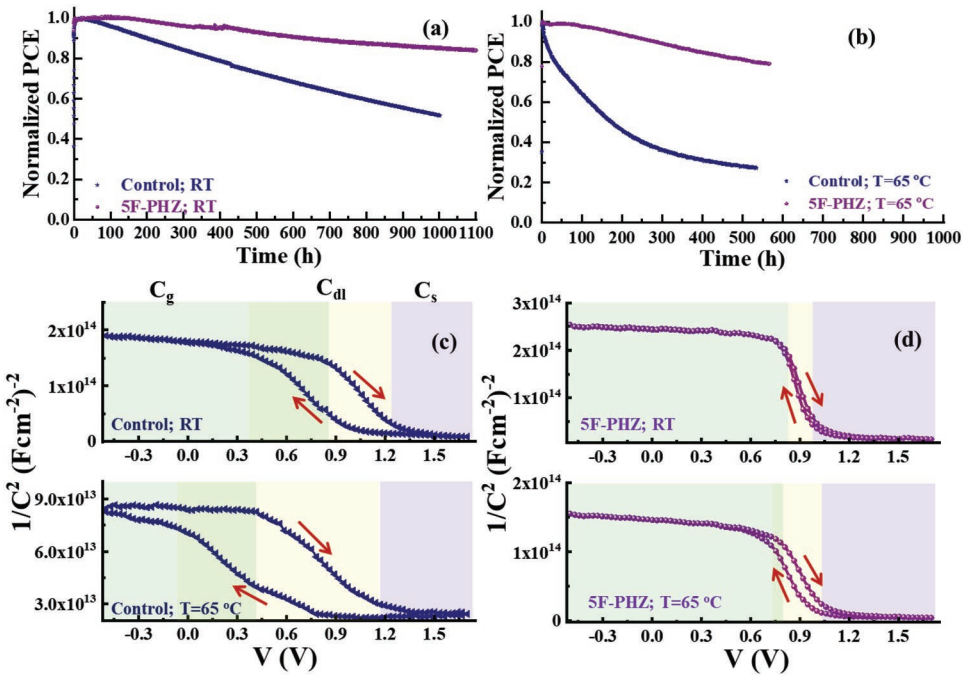

Figure 6. Operational stability of the control and 5F-PHZ treated devices (regular perovskite (Eg ≈ 1.51–1.52 eV). The devices were placed under 1-sun intensity under MPPT conditions (35–40% RH, a) 27–32 °C ≈ RT, and b) elevated temperature ≈65 °C) during device stability monitoring. c,d) *M–S* plots of the control and 5F-PHZ treated devices aged under respective conditions. The shaded region indicates a characteristic capacitance regime. Arrows indicate forward/reverse scan direction during *C–V* data collection. Overlapped shaded regimes indicate the lagging of the *C–V* curve induced by interfacial deterioration.

It substantiates that the PSC with 5F-PHZ treatment also has better moisture resistivity. To complement this result, we measured the water contact angle to evaluate the hydrophobicity of HaP films (Figure S18b,c, Supporting Information). The control HaP film with a contact angle of 61.2° ($t_o \approx 0$ s) decreased to 38.4° after 1 min. While the 5F-PHZ treated perovskite film demonstrated a higher contact angle of 82.4° which retains to 79.6° atfer 1 min. It reveals that the 5F-PHZ treated HaP film has excellent moisture resistance. Thus, the result substantiates that the superior stability of our 5F-PHZ treated PSC is partly attributed to its higher hydrophobicity.

Furthermore, to evaluate the interfacial deterioration with aging, we collected the *C–V* responses of aged devices as depicted in Figure 6c,d. The *M–S* curves of the 5F-PHZ treated device (Figure 6d) revealed a comparatively stable intrinsic junction that stems from geometrical capacitance (C_g).[56,57] one can see a smaller *C–V* hysteresis for the aged device with 5F-PHZ at RT and 65 °C indicating mitigation of ionic motion or interfacial charge accumulation that could induce during the forward and reverse scan directions.[45,58,59] A pronounced *C–V* hysteresis for the control device with thermal stress aging suggests a less stable and defective interface compared to the 5F-PHZ treated device. This observation is parallel to our earlier report on degradation with interfacial deterioration.[6] It also shows a sharp transition of *M–S* curves suggesting a narrower depletion layer capacitance (C_{dl}) regime that could be related to low defect density. A saturated capacitance (C_s) regime for V_D is caused by charge accumulation at the interface and electrode polarization. These characteristics (Figure 6c) deteriorate with wider *C–V* hysteresis and varying V_D in the control device under operational aging. It corroborates that the control device degrades with the loss of intrinsic junction characteristics and increasing dominance of the lagging of interfacial ionic motion. Interestingly, this deleterious feature is significantly suppressed in the device with 5F-PHZ passivation (Figure 6d) which is attributed to a robust interface. Indeed, it is reported that strong halogen bonding to halide ions and the tendency of fluoroarene moieties to bind halide ions with π-anion interaction controls the ions migration.[33,38] Thus, it is speculated that a stronger interaction of fluorine bolsters the interfacial adhesion forming a robust and stable interface and hence contributes to better device stability.

3. Conclusion

In this work, we have demonstrated interfacial passivation on 3D-HaP systems to achieve highly efficient and stable inverted PSCs with sputtered NiO_x as HTL. It remarkably enhances device performance (RB-PSCs) from ≈18.10% to 22.29% with superior device stability. Indeed, this method is also applicable to PSCs with wide and narrow bandgap perovskite systems. This surface treatment with 5F-PHz significantly modifies the surface chemistry and interfacial energy band due to strong halogen bonding induced by fluoroarene moieties coated on a 3D surface. TEM analysis confirms interfacial modification with uneven distribution of 2D phase embedded at C_{60}/perovskite interface. The ToF-SIMS and XPS results revealed that the 5F-PHZ was mainly distributed on the perovskite surface with slight diffusion to the bulk via grain boundaries. The device analysis revealed that

the 5F-PHz treatment improves the optoelectronic properties coupled with a higher diffusion potential (0.984 to 1.12 V) and relatively shallower defect level $E_{t1}, E_{t2} \approx 0.254, 0.405$ eV in the control device; $E_{t1}^{'}, E_{t2}^{'} \approx 0.237, 0.378$ eV in the device with 5F-PHZ) with suppression of defect densities (N_{t1}, $N_{t2} \approx 1.36 \times 10^{17}$, 8.76×10^{16} cm^{-3} for the control device to $N_{t1}^{'}, N_{t2}^{'} \approx 3.28 \times 10^{16}$, 4.26×10^{16} cm^{-3} for the 5F-PHZ treated device). This approach significantly improves the operational stability of PSCs with simultaneous passivation of the bulk and surface of 3D perovskite film. This report underscores the halogen bonding interaction with various fluoroarene derivatives to further improve both the efficiency and operational stability of PSCs.

4. Experimental Section

Materials and Precursor Solution: All chemicals were purchased from commercial suppliers as mentioned and unless otherwise specified, they were used as received. Formamidinium iodide (FAI, GreatCells), 5-Ammonium valeric acid iodide (5-AVAI, TCI), pentafluoro-phenylhydrazine (5F-PHZ) (TCI, 98.5%), PbI_2 (Wako Chemicals, 98.5%), $PbBr_2$ (TCI, ≥98.5%), SnI_2 (Sigma Aldrich, 99.999%), SnF_2 (Sigma Aldrich, 99.99%), MASCN (TCI, ≥98.5), [2-(3,6-Dimethoxy-9*H*-carbazol-9-yl)ethyl]phosphonic Acid (MeO-2PACz) (TCI), PEDOT:PSS (AI 4083, Heraeus) C_{60} (TCI, 99%), C_{60}-fused N-methylpyrrolidine-meta-dodecyl phenyl ($C_{60}MC_{12}$) (TCI, 99% purity) and Bathocuproine (BCP) (Sigma Aldrich, 99% purity) were purchased and used as received.

Preparation of MA-free RB-HaP; $FA_{0.84}Cs_{0.12}Rb_{0.04}PbI_3$: MA-free regular bandgap halide perovskite (RB-HaP): the precursor solution (1.05 M) was prepared by dissolving FAI (0.84 M), CsI (0.12 M), RbI (0.04 M), PbI_2 (1 M), and 5-AVAI (1 mM) in the mixture of dimethylformamide (DMF), and dimethyl sulfoxide (DMSO) (4:1) solvent for 2 h at 70 °C temperature. For film deposition, the precursor was spin-coated at 1000 rpm for 10 s (ramping slope 2 s) and 5000 rpm for 40 s followed by dripping 800 µl of CB at the 34th s of the second step. Then to promote the crystallization, those as-grown films were simply placed on a hot plate at 60 °C for 1 min and at 100 °C for 45 min. For surface passivation, 5F-PHZ precursor solutions of different concentrations (0.5–10 mol% ml^{-1}) were prepared by dissolving in isopropyl alcohol (IPA) at 60 °C for 2 h. For surface treatment with 5F-PHZ, the 5F-PHZ solution was spin-coated onto the HaP film at 5000 rpm for 40 s (ramping slope 3 s) and annealed at 100 °C for 5 min.

Preparation of MA-free WB-HaP; $FA_{0.84}Cs_{0.12}Rb_{0.04}Pb(I_{0.63}Br_{0.37})_3$: Wide bandgap halide perovskite (WB-HaP): the precursor solution (1 M) was prepared by dissolving FAI (0.84 M), CsI (0.12 M), RbI (0.04 M), PbI_2 (0.45 M), $PbBr_2$ (0.55 M), and 5-AVAI (1 mM) in 1 ml of a mixture of DMF and DMSO (4:1) solvent for 2 h at room temperature. Note that in the device, cations composition was adopted as in regular MA-free PSCs while the halide composition was taken with the reference of MA-free WB-HaP reported by the Snaith group[60] and the previous report.[51] For film deposition, the precursor was spin-coated at 1000 rpm for 10 s (ramping slope 2 s) and 5000 rpm for 40 s followed by dripping 800 µl of CB at the 42nd s of the second step. Then to promote the crystallization, those as-grown films were simply placed on a hot plate at 60 °C for 1 min and at 100 °C for 45 min. For surface treatment with 5F-PHZ, the 5F-PHZ solution in IPA was spin-coated onto the HaP film at 5000 rpm for 40 s (ramping slope 3 s) and annealed at 100 °C for 5 min.

Preparation of NW-HaP; $FA_{0.85}MA_{0.1}Cs_{0.05}(Pb_{0.5}, Sn_{0.5})I_3$: Narrow bandgap halide perovskite (NB-HaP): the precursor solution (1.4 M) was prepared by dissolving FAI (0.85 M), MAI (0.1 M), CsI (0.05 M), PbI_2 (0.5 M), SnI_2 (0.5 M), SnF_2 (0.05 M), and MASCN (0.05 M) in the mixture of DMF and DMSO (4:1) solvent for 1 h at 50 °C temperature. Note that the NB-HaP; $Cs_{0.05}MA_{0.1}FA_{0.85}(Pb_{0.5}, Sn_{0.5})I_3$; the composition was inspired from a report by Yanfa Yan and co-workers.[55] Though the report used a two-step process, a single precursor solution was used for the preparation of NB-HaP film. For film deposition, the precursor was spin-coated at 5000 rpm for 50 s (ramping slope 3 s) followed by dripping 150 µl of CB at the 20th s of the second step. Then, deposited films were placed on a hot plate at 60 °C for 2 min and at 100 °C for 10 min. For surface treatment with 5F-PHZ, the 5F-PHZ solution in IPA was spin-coated onto the HaP film at 5000 rpm for 40 s (ramping slope 3 s) and annealed at 100 °C for 5 min.

All the solutions were filtered using 0.2 µm syringe filters just before the deposition to avoid the risk of unwanted particles in the precursor solution.

Perovskite Solar Cell Fabrication: The p-i-n device structure for all perovskite systems was fabricated. Solar cell devices were fabricated on pre-cleaned patterned indium tin oxide (ITO) coated glass substrates (15 Ω sq.$^{-1}$). The ITO substrates were pre-cleaned in an ultrasonic bath with detergent, pure water, and 2-propanol, followed by a UV-ozone treatment for 5 min to remove the organic residuals. The NiO_x (~20 nm) film was deposited by sputtering as mentioned in the earlier reports.[6] In brief, the pre-cleaned ITO substrates were loaded in the deposition chamber and evacuated until $< 2 \times 10^{-3}$ Pa then pure argon gas was introduced at the rate of 20 sccm. The deposition was carried out in an argon gas pressure of 3.5 Pa and RF power supply of 150 W for 10 min at room temperature. NiO_x target (99.9% pure) was used from Kojundo Chemical Laboratory Co. Ltd, Japan. Then substrates were transferred into a nitrogen-filled glove box (< 1.0 ppm O_2 and H_2O) and the rest of the steps were carried out inside the glove box. The sputtered NiO_x thin film was treated with MeO-2PACz by spin coating at 5000 rpm for 50 s and subsequently dried at 100 °C for 10 min on a hot plate. Note that PEDOT:PSS had been used as HTL (diluted by methanol by 1:1, spin-coated by 3000 rpm for 50 s, and annealed at 140 °C for 20 min on a hot plate) as described in the earlier reports.[44,49] The films of RB-HaP, WB-HaP, and NB-HaP perovskites were grown onto the ITO/HTL substrate as described above. Note that the RB-HaP and WB-HaP were grown onto the ITO/NiOx/MeO-2PACz substrates while the NB-HaP films were prepared on ITO/PEDOT:PSS substrate. The target films were prepared with 5F-PHZ treatment as described above. For RB-PSCs and NW-PSCs, C_{60} (26 nm at 0.1 Å s^{-1}) by thermal evaporation was deposited while $C_{60}MC_{12}$ (2 wt%, CB) was spin-coated as an electron transport layer (ETL). After that, the electron selective layer (ESL), BCP (6 nm, at 0.1 Å s^{-1}) was deposited by evaporation at a base pressure of $\approx 5 \times 10^{-4}$ Pa. Then, to complete the device structure, samples were then transferred into the evaporation chamber connected to the glove box for metal contact deposition. Finally, 130 nm of Ag was thermally evaporated at a pressure $< 10^{-4}$ Pa. Devices with an area of ≈1 cm^2 were sealed using UV-curable resins before the subsequent measurements in ambient conditions.

Materials and Device Characterizations: XRD patterns of fabricated Sn-HaP films were collected using an advanced XRD (Rigaku SmartLab, CuK_α radiation, λ = 1.54050 A) Bragg-+Brentano θ-2θ configuration at room temperature. The morphology of films and cross-sectional images were taken by a high-resolution scanning electron microscope (SEM) at 5 kV accelerating voltage (Hitachi, S-4800). The absorption spectra and photoluminescence (PL) spectra of various films were measured using UV–vis–NIR spectrometer (UV-2600i, Shimadzu) and micro-PL spectrometer (HORIBA, LabRamHR-PL NF(UV–NIR)) equipped with ≈532 nm laser diode (10 mWcm^{-2}) as an excitation source. The carrier lifetimes were measured with a fluorescence lifetime spectrometer (Quantaurus-τ from Hamamatsu-Photonics K.K., C11367) equipped with a ≈405 nm laser diode (typical peak power of 400 mW) at a 200 kHz repetition rate.

XPS spectra were obtained using a Versa Probe II (ULVAC-PHI, Japan). Perovskite film samples for XPS measurements were prepared in an N_2-filled glove box and transferred to the XPS chamber through an N_2-filled transfer vessel in order to avoid oxygen contamination. XPS with a nonmonochromatic source was measured (Al Kα; 1486.6 eV, spot size 10–300 µm) at pass energy of 187.85 eV (1.5 eV step size) for the survey scan and pass energy 46.95 eV (0.1 eV step size) for the fine scan with spot size 100 µm. The XPS spectra were calibrated with the binding energy of 284.8 eV for C1s. The band structure of the film was measured

using UPS (Thermo Fisher Scientific, Inc.) with a He I line (21.2 eV) from a helium discharge lamp. The surface hydrophobicity of perovskite film was measured using contact angle measurements (Drop Master DM300, Kyowa Interface Science, Niiza, Japan). Briefly, a 1.6 µL drop of deionized water was placed on the perovskite surface and the mean initial contact angle values of three different spots were determined.

ToF-SIMS measurements were carried out using a nanoTOF (PHI TRIFT V) instrument equipped with a 30 keV Bi_3^{2+} beam for analysis. For sample etching, a 1 keV, 50 nA Ar gun was used for sputtering. Primary ion dose density (PIDD) was maintained at less than approximately 2–3 × 10^{11} ions cm^{-2} in each measurement cycle to prevent sample damage from the irradiation of the primary ion beam. The sputtering area of the sputtering ion beam was 500 × 500 µm and the raster area of the primary ion beam was 100 × 100 µm.

The samples for TEM were prepared by using a focused ion beam (FIB) technique (JEOL, JIB-4501) inside a glove box. Before the sample preparation with the FIB, a thin layer of osmium and carbon was deposited on the top of the sample (the Ag layer peeled off) to protect it from damage during milling. Sample extraction was performed with a FIB accelerating voltage of 30 kV and a current of 800 pA. Once the lamella was extracted and welded on the Mo grid, it was thinned to electron transparency at 10 kV and 10 pA. The SEM accelerating voltage was kept at 5 kV for the entire process. The TEM samples were about 50–60 nm thick. The finished TEM was immediately transferred for TEM analysis to limit overall exposure to air to < 2 min. STEM/EDX was carried out at room temperature (≈300 K) using an analytical TEM (JEOL JEM-ARM200F for HR, a 200 kV acceleration voltage) equipped with a cold-field emission gun and a JEOL EDX detector. To minimize the damage from the electron beam, the exposure time was limited to within 5 s in every TEM observation.

The *J–V* curves were measured at the scan rate of 0.05 V s^{-1} under one sun with an AM1.5G spectral filter (100 mW cm^{-2}) coupled with an MPPT system (Systemhouse Sunrise Corp.). The light intensity was calibrated by a silicon (Si) diode (BS-520BK). For the stability test, the encapsulated devices were measured at MPPT conditions. The *J–V* curves were measured with a scan rate of 0.05 V s^{-1} under one sun with an AM 1.5G spectral filter (100 mW cm^{-2}) coupled with an MPPT system (Bunkoukeiki Corp. The devices were kept under 1-sun intensity under MPPT conditions (35–40% RH, 27–32 °C ≈ RT; elevated temperature ≈65 °C; 60–65% RH, RT) during device stability monitoring. BIR-50 solar cell light resistance test system, incubator type 50 × 50 mm irradiation, Systemhouse Sunrise Corp.). The external quantum efficiency (EQE) spectra were obtained using a spectrometer (SM-250IQE, Bunkokeiki, Japan).

The transient photovoltage was measured using a commercial PAIOS system (PAIOS V.4.3). A pulse intensity was used to induce a spike in photovoltage. The capacitance spectra (*C–f*) were taken from PAIOS v. 4.3 software, which scans from 20 Hz to 2 MHz at 30 mV AC in the dark at a bias voltage of 0 V. The *C–V* measurements were taken at 10 kHz with a voltage amplitude of 30 mV AC in the dark. The scan frequency is determined from the plateau region (corresponds to C_g) of the capacitance-frequency spectra *C–f* scan at zero bias. The *C–f–T* spectra were measured using an LCR meter (IM3536, Hioki), the voltage amplitude of 30 mV under dark conditions in the temperature range of 253–353 K. The temperature was varied by using the controlled chamber (SU-221) (±0.1 K).

Solar Cell Certification: Device certification was conducted at the National Institute of Advanced Industrial Science and Technology (AIST), Japan. It is registered as ISO/IEC 17 025 accreditation laboratory (IA Japan ASNITE 0021 Calibration) according to international mutual recognition arrangements (MRA) for international laboratory (ILAC), and Asia pacific accreditation cooperation (APAC).

First-Principles Calculation: Density functional theory (DFT) calculations were performed using the Vienna ab initio simulation package (VASP),[61] which implements the projector-augmented wave (PAW) method.[62,63] For the exchange-correlation potential, the Perdew–Burke–Ernzerhof functional for solid (PBEsol)[64] was used together with the D4 dispersion correction.[65] The $\sqrt{2} \times \sqrt{2} \times 2$ slab supercells of (001) surface were built from a bulk tetragonal phase of $FAPbI_3$ (space group: P4/mbm), where a vacuum region of ≈30 Å was added in the *z*-direction. The dipole correction was also included in the calculation of energies and electronic structures. The kinetic cutoff energy of 500 eV and the convergence criterion of 10^{-6} eV for the self-consistent loop were employed. To investigate the various passivation effects by molecules, PbI_2-terminated surface was considered. The internal coordinates of atoms in the top five layers were fully relaxed, whereas the atoms in the bottom four layers were kept fixed. For the Brillouin zone integration, the gamma point sampling was employed for the structural relaxation, and the $3 \times 3 \times 1$ and $4 \times 4 \times 2$ *k* points were used for the subsequent SCF and DOS calculations, respectively. The desorption energy of the molecule was evaluated as $E_f = E_{defectedsurface} + \mu_{molecule} - E_{passivatedsurface}$, where $E_{defectedsurface}$ and $E_{passivatedsurface}$ are energies of defected and passivated surfaces, respectively, and $\mu_{molecule}$ is the chemical potential of the molecule. For the $\mu_{molecule}$ values of 5F-PHZ and PHA, the total energy of each isolated molecule computed by VASP was used.

Supporting Information

Supporting Information is available from the Wiley Online Library or from the author.

Acknowledgements

This work was supported by JST-Mirai Program Grant Number JPMJMI21E6, Japan. This work was partly supported the Yazaki Memorial Foundation for Science and Technology, Japan. The authors thank Dr. Hideyuki Yasufuku and Dr. Naoya Miyauchi from Research Network and Facility Services Division, Surface and Microbeam Analysis Group, NIMS, for their kind help with ToF-SIMS measurement. The authors also thank Keisuke Shinoda and Makiko Oshida from NIMS battery research platform, for the technical support for TEM measurement. The authors are grateful to Dr. Atsuko Nagataki and Kazuo Yamaguchi from NIMS battery research platform for the technical support during XRD and XPS measurement.

Conflict of Interest

The authors declare no conflict of interest.

Data Availability Statement

The data that support the findings of this study are available in the supplementary material of this article.;

Keywords

defects, fluoroarene, halogen bonding, MA-free, surface passivation, thermal stability

Received: June 16, 2022
Published online: August 17, 2022

[1] A. Kojima, K. Teshima, Y. Shirai, T. Miyasaka, *J. Am. Chem. Soc.* **2009**, *131*, 6050.
[2] H. Min, D. Y. Lee, J. Kim, G. Kim, K. S. Lee, J. Kim, M. J. Paik, Y. K. Kim, K. S. Kim, M. G. Kim, T. J. Shin, S. Il Seok, *Nature* **2021**, *598*, 444.

[3] S.-H. Turren-Cruz, A. Hagfeldt, M. Saliba, *Science* **2018**, *362*, 449.
[4] W. Tress, K. Domanski, B. Carlsen, A. Agarwalla, E. A. Alharbi, M. Graetzel, A. Hagfeldt, *Nat. Energy* **2019**, *4*, 568.
[5] T. Matsui, T. Yamamoto, T. Nishihara, R. Morisawa, T. Yokoyama, T. Sekiguchi, T. Negami, *Adv. Mater.* **2019**, *31*, 1806823.
[6] D. B. Khadka, Y. Shirai, M. Yanagida, K. Miyano, *ACS Appl. Energy Mater.* **2021**, *4*, 11121.
[7] M. Stolterfoht, C. M. Wolff, J. A. Márquez, S. Zhang, C. J. Hages, D. Rothhardt, S. Albrecht, P. L. Burn, P. Meredith, T. Unold, D. Neher, *Nat. Energy* **2018**, *3*, 847.
[8] G. Yang, Z. Ren, K. Liu, M. Qin, W. Deng, H. Zhang, H. Wang, J. Liang, F. Ye, Q. Liang, H. Yin, Y. Chen, Y. Zhuang, S. Li, B. Gao, J. Wang, T. Shi, X. Wang, X. Lu, H. Wu, J. Hou, D. Lei, S. K. So, Y. Yang, G. Fang, G. Li, *Nat. Photonics* **2021**, *15*, 681.
[9] Y. Zou, Y. Cui, H.-Y. Wang, Q. Cai, C. Mu, J.-P. Zhang, *Nanotechnology* **2019**, *30*, 275202.
[10] Y. Liu, S. Akin, L. Pan, R. Uchida, N. Arora, J. V. Milić, A. Hinderhofer, F. Schreiber, A. R. Uhl, S. M. Zakeeruddin, A. Hagfeldt, M. I. Dar, M. Grätzel, *Sci. Adv.* **2019**, *5*, aaw2543.
[11] K. T. Cho, Y. Zhang, S. Orlandi, M. Cavazzini, I. Zimmermann, A. Lesch, N. Tabet, G. Pozzi, G. Grancini, M. K. Nazeeruddin, *Nano Lett.* **2018**, *18*, 5467.
[12] F. Zhang, H. Lu, J. Tong, J. J. Berry, M. C. Beard, K. Zhu, *Energy Environ. Sci.* **2020**, *13*, 1154.
[13] A. A. Sutanto, N. Drigo, V. I. E. Queloz, I. Garcia-Benito, A. R. Kirmani, L. J. Richter, P. A. Schouwink, K. T. Cho, S. Paek, M. K. Nazeeruddin, G. Grancini, *J. Mater. Chem. A* **2020**, *8*, 2343.
[14] L. Fu, H. Li, L. Wang, R. Yin, B. Li, L. Yin, *Energy Environ. Sci.* **2020**, *13*, 4017.
[15] A. Q. Alanazi, D. J. Kubicki, D. Prochowicz, E. A. Alharbi, M. E. F. Bouduban, F. Jahanbakhshi, M. Mladenović, J. V. Milić, F. Giordano, D. Ren, A. Y. Alyamani, H. Albrithen, A. Albadri, M. H. Alotaibi, J. E. Moser, S. M. Zakeeruddin, U. Rothlisberger, L. Emsley, M. Grätzel, *J. Am. Chem. Soc.* **2019**, *141*, 17659.
[16] M. I. Saidaminov, J. Kim, A. Jain, R. Quintero-Bermudez, H. Tan, G. Long, F. Tan, A. Johnston, Y. Zhao, O. Voznyy, E. H. Sargent, *Nat. Energy* **2018**, *3*, 648.
[17] D. B. Khadka, Y. Shirai, M. Yanagida, T. Masuda, K. Miyano, *Sustainable Energy Fuels* **2017**, *1*, 755.
[18] J. Zhu, S. Park, O. Y. Gong, C. Sohn, Z. Li, Z. Zhang, B. Jo, W. Kim, G. S. Han, D. H. Kim, T. K. Ahn, J. Lee, H. S. Jung, *Energy Environ. Sci.* **2021**, *14*, 4903.
[19] Y.-H. Lin, N. Sakai, P. Da, J. Wu, H. C. Sansom, A. J. Ramadan, S. Mahesh, J. Liu, R. D. J. Oliver, J. Lim, L. Aspitarte, K. Sharma, P. K. Madhu, A. B. Morales-Vilches, P. K. Nayak, S. Bai, F. Gao, C. R. M. Grovenor, M. B. Johnston, J. G. Labram, J. R. Durrant, J. M. Ball, B. Wenger, B. Stannowski, H. J. Snaith, *Science* **2020**, *369*, 96.
[20] Z. Wang, Q. Lin, F. P. Chmiel, N. Sakai, L. M. Herz, H. J. Snaith, *Nat. Energy* **2017**, *2*, 17135.
[21] H. Kim, S. Lee, D. Y. Lee, M. J. Paik, H. Na, J. Lee, S. Il Seok, *Adv. Energy Mater.* **2019**, *9*, 1902740.
[22] D. Li, Y. Huang, G. Wang, Q. Lian, R. Shi, L. Zhang, X. Wang, F. Gao, W. Kong, B. Xu, C. Cheng, S. Li, *J. Mater. Chem. A* **2021**, *9*, 12746.
[23] X. Li, C. Li, X. Zhao, Y. Zhang, G. Liu, Z. Zhang, D. Wang, L. Xiao, Z. Chen, B. Qu, *ACS Appl. Mater. Interfaces* **2021**, *13*, 4553.
[24] S. Bai, P. Da, C. Li, Z. Wang, Z. Yuan, F. Fu, M. Kawecki, X. Liu, N. Sakai, J. T.-W. Wang, S. Huettner, S. Buecheler, M. Fahlman, F. Gao, H. J. Snaith, *Nature* **2019**, *571*, 245.
[25] D. Bi, X. Li, J. V. Milić, D. J. Kubicki, N. Pellet, J. Luo, T. LaGrange, P. Mettraux, L. Emsley, S. M. Zakeeruddin, M. Grätzel, *Nat. Commun.* **2018**, *9*, 4482.
[26] H. Zhu, Y. Liu, F. T. Eickemeyer, L. Pan, D. Ren, M. A. Ruiz-Preciado, B. Carlsen, B. Yang, X. Dong, Z. Wang, H. Liu, S. Wang, S. M. Zakeeruddin, A. Hagfeldt, M. I. Dar, X. Li, M. Grätzel, *Adv. Mater.* **2020**, *32*, 1907757.
[27] K. Junghwan, S. M. I. , T. Hairen, Z. Yicheng, K. Younghoon, C. Jongmin, J. J. Woong, F. James, Q. Rafael, Y. Zhenyu, Q. L. Na, W. Mingyang, V. Oleksandr, S. E. H. , *Adv. Mater.* **2018**, *30*, 1706275.
[28] R. Wang, J. Xue, K.-L. Wang, Z.-K. Wang, Y. Luo, D. Fenning, G. Xu, S. Nuryyeva, T. Huang, Y. Zhao, J. L. Yang, J. Zhu, M. Wang, S. Tan, I. Yavuz, K. N. Houk, Y. Yang, *Science* **2019**, *366*, 1509.
[29] D. Bi, P. Gao, R. Scopelliti, E. Oveisi, J. Luo, M. Grätzel, A. Hagfeldt, M. K. Nazeeruddin, *Adv. Mater.* **2016**, *28*, 2910.
[30] K. M. M. Salim, T. M. Koh, D. Bahulayan, P. C. Harikesh, N. F. Jamaludin, B. Febriansyah, A. Bruno, S. Mhaisalkar, N. Mathews, *ACS Energy Lett.* **2018**, *3*, 1068.
[31] I. García-Benito, C. Quarti, V. I. E. Queloz, S. Orlandi, I. Zimmermann, M. Cavazzini, A. Lesch, S. Marras, D. Beljonne, G. Pozzi, M. K. Nazeeruddin, G. Grancini, *Chem. Mater.* **2018**, *30*, 8211.
[32] M. Hossain, R. Garai, R. K. Gupta, R. N. Arunagirinathan, P. K. Iyer, *J. Mater. Chem. C* **2021**, *9*, 10406.
[33] M. A. Ruiz-Preciado, D. J. Kubicki, A. Hofstetter, L. McGovern, M. H. Futscher, A. Ummadisingu, R. Gershoni-Poranne, S. M. Zakeeruddin, B. Ehrler, L. Emsley, J. V. Milić, M. Grätzel, *J. Am. Chem. Soc.* **2020**, *142*, 1645.
[34] J. Suo, B. Yang, E. Mosconi, H.-S. Choi, Y. Kim, S. M. Zakeeruddin, F. De Angelis, M. Grätzel, H.-S. Kim, A. Hagfeldt, *Adv. Funct. Mater.* **2021**, *31*, 2102902.
[35] Y. H. Park, I. Jeong, S. Bae, H. J. Son, P. Lee, J. Lee, C.-H. Lee, M. J. Ko, *Adv. Funct. Mater.* **2017**, *27*, 1605988.
[36] A. Nakane, H. Tampo, M. Tamakoshi, S. Fujimoto, K. M. Kim, S. Kim, H. Shibata, S. Niki, H. Fujiwara, *J. Appl. Phys.* **2016**, *120*, 064505.
[37] S. Yang, S. Chen, E. Mosconi, Y. Fang, X. Xiao, C. Wang, Y. Zhou, Z. Yu, J. Zhao, Y. Gao, F. De Angelis, J. Huang, *Science* **2019**, *365*, 473 LP.
[38] A. Abate, M. Saliba, D. J. Hollman, S. D. Stranks, K. Wojciechowski, R. Avolio, G. Grancini, A. Petrozza, H. J. Snaith, *Nano Lett.* **2014**, *14*, 3247.
[39] S. Gharibzadeh, P. Fassl, I. M. Hossain, P. Rohrbeck, M. Frericks, M. Schmidt, T. Duong, M. R. Khan, T. Abzieher, B. A. Nejand, F. Schackmar, O. Almora, T. Feeney, R. Singh, D. Fuchs, U. Lemmer, J. P. Hofmann, S. A. L. Weber, U. W. Paetzold, *Energy Environ. Sci.* **2021**, *14*, 5875.
[40] X. Zheng, B. Chen, J. Dai, Y. Fang, Y. Bai, Y. Lin, H. Wei, X. C. Zeng, J. Huang, *Nat. Energy* **2017**, *2*, 17102.
[41] H. Zhu, Y. Ren, L. Pan, O. Ouellette, F. T. Eickemeyer, Y. Wu, X. Li, S. Wang, H. Liu, X. Dong, S. M. Zakeeruddin, Y. Liu, A. Hagfeldt, M. Grätzel, *J. Am. Chem. Soc.* **2021**, *143*, 3231.
[42] D. Kim, H. J. Jung, I. J. Park, B. W. Larson, S. P. Dunfield, C. Xiao, J. Kim, J. Tong, P. Boonmongkolras, S. G. Ji, F. Zhang, S. R. Pae, M. Kim, S. B. Kang, V. Dravid, J. J. Berry, J. Y. Kim, K. Zhu, D. H. Kim, B. Shin, *Science* **2020**, *368*, 155.
[43] A. Matsushita, M. Yanagida, Y. Shirai, K. Miyano, *Sol. Energy Mater. Sol. Cells* **2021**, *220*, 110854.
[44] D. B. Khadka, Y. Shirai, M. Yanagida, K. Miyano, *ACS Appl. Energy Mater.* **2021**, *4*, 12819.
[45] K. Miyano, M. Yanagida, Y. Shirai, *Adv. Energy Mater.* **2020**, *10*, 1903097.
[46] D. B. Khadka, S. Kim, J. Kim, *J. Phys. Chem. C* **2016**, *120*, 4251.
[47] K. Zhang, X. Du, Z. Chen, T. Wang, Z. Yang, H. Yin, Y. Yang, W. Qin, X. Hao, *Adv. Energy Mater.* **2021**, *12*, 2103371.
[48] S. Ye, H. Rao, Z. Zhao, L. Zhang, H. Bao, W. Sun, Y. Li, F. Gu, J. Wang, Z. Liu, Z. Bian, C. Huang, *J. Am. Chem. Soc.* **2017**, *139*, 7504.
[49] D. B. Khadka, Y. Shirai, M. Yanagida, K. Miyano, *J. Mater. Chem. C* **2020**, *8*, 2307.

[50] T. Walter, R. Herberholz, C. Müller, H. W. Schock, *J. Appl. Phys.* **1996**, *80*, 4411.
[51] D. B. Khadka, Y. Shirai, M. Yanagida, T. Noda, K. Miyano, *ACS Appl. Mater. Interfaces* **2018**, *10*, 22074.
[52] M. I. Saidaminov, A. L. Abdelhady, B. Murali, E. Alarousu, V. M. Burlakov, W. Peng, I. Dursun, L. Wang, Y. He, G. Maculan, A. Goriely, T. Wu, O. F. Mohammed, O. M. Bakr, *Nat. Commun.* **2015**, *6*, 7586.
[53] K. Momma, F. Izumi, *J. Appl. Crystallogr.* **2011**, *44*, 1272.
[54] N. Liu, C. Yam, *Phys. Chem. Chem. Phys.* **2018**, *20*, 6800.
[55] C. Li, Z. Song, C. Chen, C. Xiao, B. Subedi, S. P. Harvey, N. Shrestha, K. K. Subedi, L. Chen, D. Liu, Y. Li, Y.-W. Kim, C. Jiang, M. J. Heben, D. Zhao, R. J. Ellingson, N. J. Podraza, M. Al-Jassim, Y. Yan, *Nat. Energy* **2020**, *5*, 768.
[56] H. Tsai, W. Nie, J.-C. Blancon, C. C. Stoumpos, R. Asadpour, B. Harutyunyan, A. J. Neukirch, R. Verduzco, J. J. Crochet, S. Tretiak, L. Pedesseau, J. Even, M. A. Alam, G. Gupta, J. Lou, P. M. Ajayan, M. J. Bedzyk, M. G. Kanatzidis, A. D. Mohite, *Nature* **2016**, *536*, 312.
[57] X. Zhang, J. Zhang, D. Phuyal, J. Du, L. Tian, V. A. Öberg, M. B. Johansson, U. B. Cappel, O. Karis, J. Liu, H. Rensmo, G. Boschloo, E. M. J. Johansson, *Adv. Energy Mater.* **2018**, *8*, 1702049.
[58] B. Chen, M. Yang, S. Priya, K. Zhu, *J. Phys. Chem. Lett.* **2016**, *7*, 905.
[59] M. Yanagida, Y. Shirai, D. B. Khadka, K. Miyano, *Phys. Chem. Chem. Phys.* **2020**, *22*, 25118.
[60] D. P. McMeekin, G. Sadoughi, W. Rehman, G. E. Eperon, M. Saliba, M. T. Horantner, A. Haghighirad, N. Sakai, L. Korte, B. Rech, M. B. Johnston, L. M. Herz, H. J. Snaith, *Science* **2016**, *351*, 151.
[61] G. Kresse, J. Furthmüller, *Phys. Rev. B* **1996**, *54*, 11169.
[62] G. Kresse, D. Joubert, *Phys. Rev. B* **1999**, *59*, 1758.
[63] P. E. Blöchl, *Phys. Rev. B* **1994**, *50*, 17953.
[64] J. P. Perdew, A. Ruzsinszky, G. I. Csonka, O. A. Vydrov, G. E. Scuseria, L. A. Constantin, X. Zhou, K. Burke, *Phys. Rev. Lett.* **2008**, *100*, 136406.
[65] E. Caldeweyher, C. Bannwarth, S. Grimme, *J. Chem. Phys.* **2017**, *147*, 034112.